Journal of Materials Processing Tech. 287 (2021) 116658

Contents lists available at ScienceDirect

Journal of Materials Processing Tech.

journal homepage: www.elsevier.com/locate/jmatprotec

Material modeling and simulation of continuous-bending-under-tension of AA6022-T4

Timothy J. Barrett[a], Shuhei Takagi[b], Nazrul Islam[c], Toshihiko Kuwabara[b], Tasnim Hassan[c], Brad L. Kinsey[a], Marko Knezevic[a], Yannis P. Korkolis[d,*]

[a] Department of Mechanical Engineering, University of New Hampshire, 33 Academic Way, Durham, NH, 03824, USA
[b] Department of Mechanical Systems Engineering, Tokyo University of Agriculture and Technology, 2-24-16 Naka-cho, Koganei-shi, Tokyo, 1848588, Japan
[c] Department of Civil, Construction and Environmental Engineering, North Carolina State University, 2501 Stinson Drive, Raleigh, NC, 27607, USA
[d] Department of Integrated Systems Engineering, The Ohio State University, 234 Baker Systems, 1971 Neil Avenue, Columbus, OH, 43210, USA

ARTICLE INFO

Associate Editor: J. Cao

Keywords:
Continuous-bending-under-tension
Simple tension
Ductility
AA6022-T4
Kinematic hardening
Numerical simulation

ABSTRACT

In earlier contributions, we discussed continuous-bending-under-tension (CBT) experiments on AA6022-T4. We found that CBT significantly enhanced the elongation-to-fracture and strength, over uniaxial tension. In the present paper, our understanding of CBT is expanded beyond these experimental observations, with the aid of material modeling and numerical simulations of the process. Cyclic tension-compression experiments were performed on this material, using strain histories that are expected to replicate the loading during CBT, i.e., different combinations of constant strain amplitude and linearly increasing mean value, to failure. During these experiments, a limited but not negligible amount of kinematic hardening was discovered. Some of these experiments are used for calibration of a combined isotropic-kinematic hardening model, while the rest are used for experimental validation of the model. The modeling framework is based on a rate-independent, associated flow rule with the von Mises yield criterion as the plastic potential. Isotropic hardening is introduced by a simple, exponential-decay model of the growth of the yield surface with plastic deformation. Non-linear kinematic hardening is introduced by a 4-term, Chaboche-type model. The large strain hardening curve is identified by extrapolation, an approach that is validated later in the work and contrasted with alternative options. This material modeling framework is introduced in finite element models of the CBT process. The model is meshed with linear, reduced-integration elements, with 7 elements through the thickness. It is found that the numerical model reproduces the experimental force-displacement curve, including the succession of spikes and plateaus typical of CBT, very closely. The model also replicates the development of strain on the surface during CBT, and compares well with post-test strain measurements. After these validations, the model is used to probe the mechanics of the CBT process, e.g., the development of stress and strain through the thickness and per cycle, the location and onset of failure, as well as the failure angle, which in CBT differs from the localized neck angle found in a typical uniaxial tension experiment.

1. Introduction

Continuous-bending-under-tension (CBT) is a process that has been shown to enhance the elongation-to-fracture (ETF) of a large variety of metals. In CBT, a set of three rollers reciprocates along the length of a strip that is loaded in tension (Fig. 1), thus periodically subjecting every material point to a combination of plastic bending-under-tension. Because plastic flow occurs under this mechanism, which is not favorable to necking, the latter can be suppressed and very large strains can be induced before the intrinsic ductility of the material is exhausted and failure occurs. This leads to an enhanced ETF in CBT over uniaxial tension (UT). Indeed, in a recent investigation, (Poulin et al., 2019) found that ETF in CBT of a dual-phase steel was increased five times over that in UT.

The superposition of stretching and bending is common in sheet metal forming, and as such it is treated even in textbooks. Among others, the seminal work of (Hu et al., 2002) considers not only bending of sheet, but also combined bending and stretching, and bending and unbending under tension, a problem of relevance in drawbead behavior. However, limited work exists in the problem of cyclic bending-unbending under tension, such as the CBT process examined here. In the same spirit, though there is extensive work on localization under in-

---

[*] Corresponding author.
E-mail address: Korkolis.1@osu.edu (Y.P. Korkolis).

https://doi.org/10.1016/j.jmatprotec.2020.116658
Received 28 May 2019; Received in revised form 9 February 2020; Accepted 21 February 2020
Available online 22 February 2020

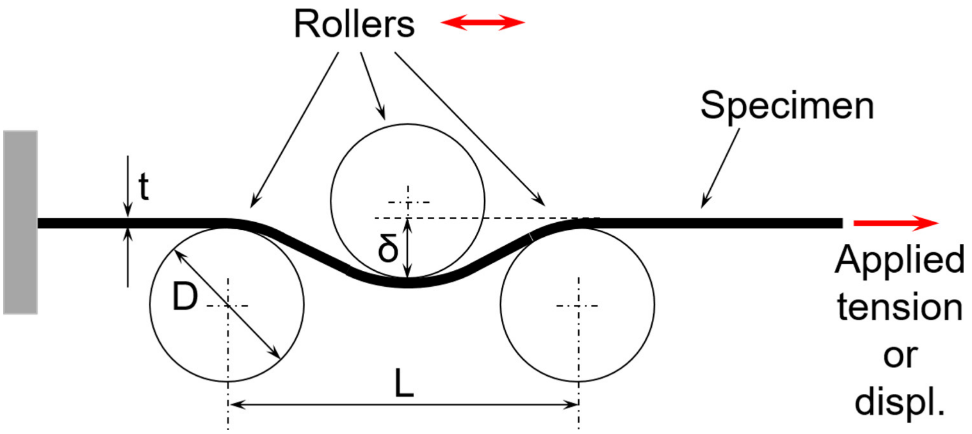

Fig. 1. Schematic of the continuous-bending-under-tension (CBT) process and definition of key variables.

plane stretching (Marciniak and Kuczyński, 1967) and the effects of bending (Marciniak and Kuczyński, 1979) there is limited work on the effect of cyclic bending-under-tension.

The CBT process belongs to a family of "stabilized tensile tests" (Emmens, 2011) for the reason described above and some macroscopic resemblance to uniaxial tension. The method was proposed by (Benedyk et al., 1971) as a way to obtain the large-strain response of materials. It then remained in relative obscurity (Benedyk et al., 2002) until it was revisited by (Emmens and van den Boogaard, 2009), partly to explain the enhanced formability during incremental forming: (Emmens and van den Boogaard, 2009) found that the actual bending radius is the most influencing factor, which in turn is controlled by the pulling force and the bending angle. They found a lesser effect of the thickness. (Emmens and van den Boogaard, 2011) presented and verified a simple mechanical model incorporating non-constant bending radius and cyclic material behavior. They also proposed a stability parameter. Interestingly, they concluded that many of the results observed are determined by the test method, and are as such independent of the material tested. Finally, (Emmens and van den Boogaard, 2012) described a way of using CBT to identify the hardening curve at large strains.

The process is under investigation by the authors for about 5 years. In earlier contributions the authors described observations in CBT of the automotive aluminum alloy AA6022-T4. (Roemer et al., 2015) found that CBT enhanced the ETF and reduced the axial force. The latter was sometimes found to be even below the yield limit of the material (see (Momanyi et al., 2017; Roemer, 2016)), which is explained because the material flows plastically due to the combination of bending and tension. (Roemer et al., 2019) reported observations of strain on the surface of the specimen, which revealed that the CBT strain paths are very close to those of UT – but reaching significantly higher levels – at least for the range of process parameters (e.g., bending depth) explored. This was corroborated by the microstructural observations presented in (Zecevic et al., 2016b), which revealed that the texture development in CBT is very similar to the one in UT, especially inside the neck of a fractured UT specimen; a strong < 111 > fiber texture was found throughout the material after CBT. Lastly, (Benedyk et al., 2015) revisited the process and discussed potential automotive applications.

In contrast to the similarity in texture development, (Knezevic et al., 2019) found that the formation of dislocation substructures during CBT is different from UT. Their study found that dislocation structures form within grains during UT and that they are disorganized and not as well defined. In contrast, cellular substructures were observed to form very early during CBT processing, even after the first cycle and to evolve from loose tangles of dislocations to well-defined walls during subsequent cycles. These dislocation patterns are responsible for the significant strengthening of the alloy during CBT.

Attempts to use the CBT to identify the hardening curve of AA6022-T4 at large strains were thwarted by the spatially non-uniform stress and strain fields that naturally arise in CBT (e.g., through-thickness variation due to bending and axial variation due to roller travel limits). Moreover, the strength of the material after CBT processing is not only determined by the achieved effective strain level, but also dependent on the specific conditions during the CBT test, inducing specific microstructural evolution. Therefore, estimating the post-necking material behavior based on measurements of the effective strain level and tensile strength by interrupting CBT tests after a certain number of cycles is not possible for the alloy. However, (Knezevic et al., 2019) showed that the extrapolation of tensile material behavior to strain levels higher than achievable with UT alone is possible by matching the measured load-displacement data during CBT by FE simulations of the process.

Another aspect of material behavior that has to be taken into account in modeling of CBT is the behavior under cyclic loading. This is typically captured by kinematic hardening (KH) models. The approach followed in this work is the one proposed by (Lemaitre and Chaboche, 1990), who modified the Armstrong-Frederick non-linear KH model by adding multiple backstress terms. In a two-paper investigation, Hassan and Kyriakides examined the behavior of numerous KH models, including the one by (Dafalias and Popov, 1975) under uniaxial (Hassan and Kyriakides, 1992) and multiaxial (Hassan et al., 1992) cyclic loading. Additional complications arise in KH investigations of thin sheets, as in this work, due to the challenges in reverse loading, since the sheet will readily buckle. (Geng et al., 2002) examined the ability of a reverse-bend test to probe KH but found that it could not be post-processed unambiguously. Subsequently, (Boger et al., 2005) used an anti-buckling device adapted to a universal testing machine to successfully perform compression of thin sheets to over 0.20 strain. The use of that device to high temperatures was extended by (Piao et al., 2012). In parallel, (Chung et al., 2005) developed a modified Chaboche-type KH framework to account for the Bauschinger effect and transient behavior measured on metal sheets (Lee et al., 2005). In other approaches, (Yao and Cao, 2002) introduced a backstress tensor and a changing exponent of the yield function to model the evolution of the yield locus and used it to predict the forming limit diagrams in in-plane stretching. (Cao et al., 2009) described a different antibuckling device and used the results to propose KH laws based on modifications of Chaboche, Dafalias-Popov and Krieg models. Lastly, (Yoshida et al., 2002) proposed a way to perform reverse loading tests by gluing together multiple sheet specimens, and used it to propose a KH model based on the concept of bounding surfaces (Yoshida and Uemori, 2002).

There are few previous works on numerical analysis of CBT. (Hadoush et al., 2011) developed a 3D finite element (FE) model using triangular shell elements based on the discrete Kirchhoff theory. Their numerical model was used to analyze the force-displacement curve and assess the stability of the CBT process. The DC06 steel was modeled using three different sets of material parameters, one isotropic hardening (IH) model and two combined isotropic-kinematic hardening (CIKH) models. They observed that these material models gave similar predictions of force-displacement during the stable portion of the test, while producing different predictions for the onset of failure. (Nikhare et al., 2012) also performed FE simulations on DC06 steel undergoing the CBT process. The CBT process was modeled using 3D linear elements to assess the residual formability of interrupted CBT tests. Their numerical analysis showed the benefits of using an extended roller stroke over a fixed roller stroke. It was seen that the formability was considerably increased with a large number of CBT cycles due to the uniform deformation that occurred along the gage length of the specimen.

2. Cyclic and large-strain behavior of AA6022-T4

2.1. Continuous tension-compression experiments

During CBT, the material undergoes cyclic bending under tension, with the bending strain amplitude remaining constant and the axial strain continuously increasing. A complication arises from the fact that the strains increase to very high levels (Benedyk et al., 1971; Emmens and van den Boogaard, 2012; Roemer et al., 2019; Zecevic et al., 2016b). To replicate this behavior, albeit to moderate strains, a series of custom cyclic experiments are performed, using the apparatus shown in Fig. 2a. In that machine, a hydraulic actuator (A, in Fig. 2a) is applying the axial force to the specimen, setting it to tension or compression in a continuous fashion. To prevent buckling of the thin-sheet specimen during compression, a set of dies (B, in Fig. 2a, and zoomed-in in Fig. 2b) are continuously enveloping the specimen. The dies are able to move relative to each other along the loading direction thanks to the comb-shaped features shown in Fig. 2b (Deng et al., 2018; Kuwabara, 2014; Zecevic et al., 2016a). The dies are held together by a second hydraulic actuator (C, in Fig. 2a), which applies the blank-holding force. The specimen geometry is shown in Fig. 2c.

The blank-holding force is maintained at 3.7 kN during the experiments, which induces a through-thickness stress of 1.85 MPa, or less than 2% of the yield stress of the material (Roemer et al., 2019). The effect of friction on the results is compensated by performing runs under the same parameters but without a specimen installed. The cross-head displacement is 0.055 mm/s, which induces a strain-rate of 5×10^{-4} /s in the test-section. The strain is continuously measured using high-elongation strain-gages (Kyowa YFLA-2-1 L).

Since it was uncertain what the exact strain histories that material points experience during CBT would be, it was decided to perform multiple types of cyclic experiments, see Fig. 3 and Table 1. As discussed in the next section, and shown in Table 1, one of these experiments (RD06, with the largest strain range hysteresis loop) is used for calibrating the constitutive model and the rest are used for model validation. The common feature of the strain histories shown in Fig. 3 is the constant strain amplitude with a linearly-increasing mean value. In some of the experiments (e.g., RD12) the strain amplitude is smaller than in others (e.g., RD11 and RD13), but the mean value rises faster. Also included are experiments where there are only two load reversals and the specimen is then loaded to failure (e.g., RD04).

2.2. Implementation of a non-linear kinematic hardening model

The combined isotropic – nonlinear kinematic hardening model as implemented in ABAQUS is used for simulation of the CBT experimental responses presented in (Roemer et al., 2019). First, the constitutive model is experimentally validated against the material-level, experimental responses discussed above in Section 2.1. A few of the experimental responses described in Section 2.1 (see Table 1) are used to calibrate the CIKH model. The constitutive model is subsequently used to simulate the remaining material responses as experimental validation, before using it in CBT simulations.

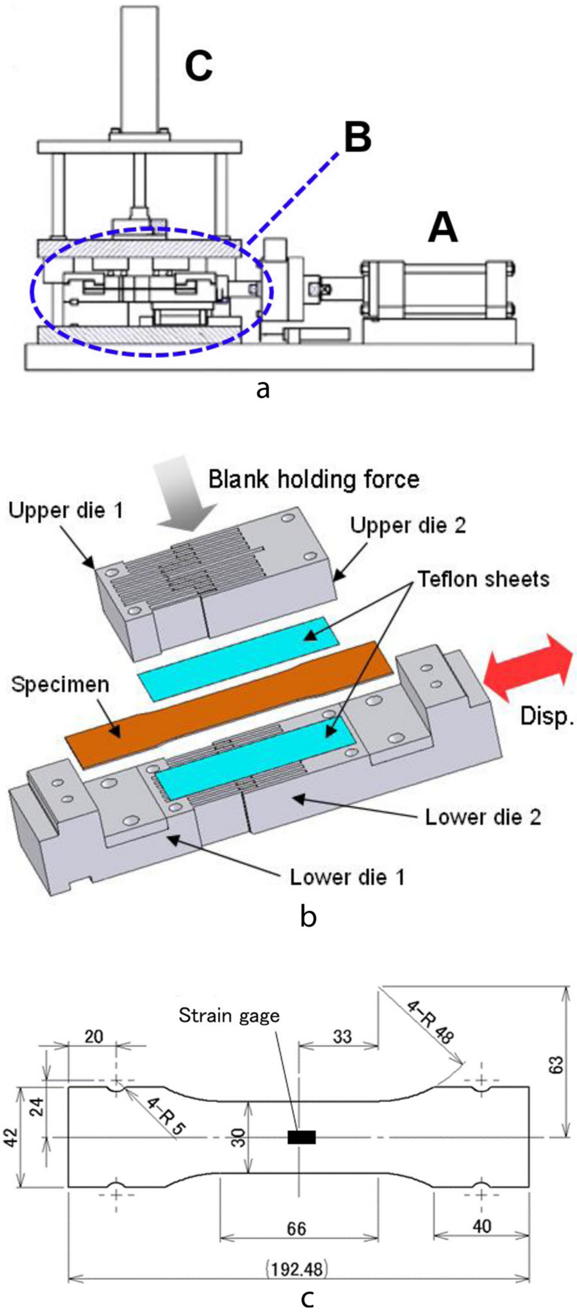

Fig. 2. (a) Schematic of the tension-compression testing machine, showing the specimen and the comb-shaped dies to prevent buckling. (b) Close-up of the comb-shaped dies. (c) Drawing of the tension-compression specimen.

The modeling framework used is based on a rate-independent, associated flow-rule with the von Mises (i.e., J_2) yield criterion, f, as the plastic potential. The flow-rule of the model indicates that the plastic strain-rate tensor $\dot{\varepsilon}^p$ is derived from the plastic potential f as follows:

$$\dot{\varepsilon}^p = \frac{\partial f(\boldsymbol{\sigma} - \boldsymbol{\alpha})}{\partial \boldsymbol{\sigma}} \dot{p} \tag{1}$$

where the von Mises yield criterion is given by:

$$f(\boldsymbol{\sigma} - \boldsymbol{\alpha}) = J_2(\boldsymbol{\sigma} - \boldsymbol{\alpha}) - \sigma_o - R = \sqrt{\frac{3}{2}(\boldsymbol{s} - \boldsymbol{a}) : (\boldsymbol{s} - \boldsymbol{a})} - \sigma_o - R \tag{2}$$

and $\boldsymbol{\sigma}$ and $\boldsymbol{\alpha}$ are the stress and back-stress tensors, $\boldsymbol{s}$ and $\boldsymbol{a}$ are their deviatoric components, respectively, σ_o is the initial yield stress and R its change during plastic deformation, and $\dot{p}$ the equivalent plastic

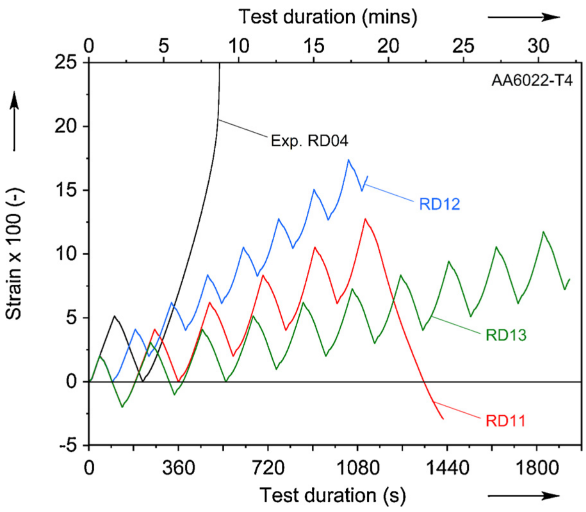

Fig. 3. Strain histories in the cyclic tension-compression experiments.

Table 1
Cyclic plasticity experiments.

#	Name of test	Test parameters (strain limits)	Comments
1	RD03	Tension to 1%, compression to 0%, tension to failure	For verification
2	RD04	Tension to 5%, compression to 0%, tension to failure	For verification
3	RD05	Tension to 10%, compression to 0%, tension to failure	For verification
4	RD06	Tension to 15%, compression to 0%, tension to failure	**For calibration**
5	RD11	Strain amplitude = 4%, mean strain increase = 2% per cycle, to failure (i.e., 0 – 2 – (−2) – 4 – 0 – 6 – 2 – etc.)	For verification
6	RD12	Strain amplitude = 2%, mean strain increase = 2% per cycle, to failure (i.e., 0 – 2 – 0 – 4 – 2 – 6 – 4 – 8 – 6 – etc.)	For verification
7	RD13	Strain amplitude = 4%, mean strain increase = 1% per cycle, to failure (i.e., 0 – 2 – (−2) – 3 – (−1) – 4 – 0 – 5 – 1 – 6 – 2 – etc.)	For verification

strain-rate (used in the current, rate-independent analysis, as a rate-independent parameter, i.e., the increment of equivalent plastic strain). The use of a rate-independent model is well-justified for this material and at the range of strain-rates encountered in CBT (Roemer et al., 2019). The center of the yield surface is assumed to translate according to a 4-term Chaboche-type, non-linear kinematic hardening model (Chaboche, 1986; Deng et al., 2018):

$$\boldsymbol{\alpha} = \sum_{i=1}^{4} \boldsymbol{\alpha}_i \tag{3}$$

where each term $\boldsymbol{\alpha}_i$ evolves according to:

$$\dot{\boldsymbol{\alpha}}_i = C_i \, \dot{p} \, \frac{\boldsymbol{\sigma} - \boldsymbol{\alpha}}{\sigma_o + R} - \gamma_i \, \boldsymbol{\alpha}_i \, \dot{p} \tag{4}$$

In these equations, C_i and γ_i are parameters determined using a stress-strain hysteresis curve. It is noted here that in ABAQUS the right hand side of the kinematic hardening rule in Eq. (4) is written a little differently than the original (Chaboche, 1986) model. However, this difference doesn't introduce any variations in the simulation responses.

In addition to kinematic hardening, it was found necessary to change the size of the yield surface (isotropic hardening) according to a simple exponential decay law (Chaboche, 1986; Deng et al., 2018):

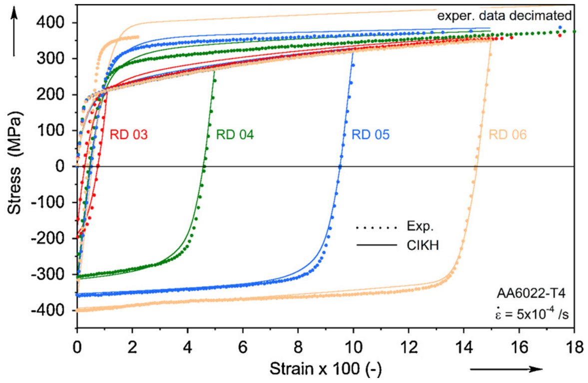

Fig. 4. Tension-compression-tension experiments and the behavior of the combined isotropic-kinematic hardening (CIKH) model calibrated from this data.

$$R = R_{max}\,(1 - e^{-bp}) \tag{5}$$

where R_{max} is the maximum expansion of the yield surface and b is a parameter that controls the decay rate of the expansion of that surface.

The present modeling framework has ten independent variables: σ_o, b, and 4 pairs of C_i and γ_i. The first two are the IH rule parameters and the remaining eight are the kinematic hardening rule parameters. These parameters are calibrated by simulating the compressive hysteresis curve with the largest strain range (RD06 hysteresis curve, shown in Fig. 4). First, each of the parameters are estimated manually using the procedure in (Bari and Hassan, 2000). Following that, the parameters are refined for improved simulation of the hysteresis curve of RD06 experiment as shown in Fig. 4. The parameters thus determined are listed in Table 2.

2.3. Experimental validation of the constitutive model

The constitutive model is experimentally validated by simulating the remaining material experiments presented in Section 2.1 using the parameter set from Table 2. The simulations of RD03, RD04, RD05 and RD06 responses are shown in Fig. 4 to be quite satisfactory for the compressive hysteresis curves, whereas the tensile hysteresis curves are in most cases slightly overpredicted. Note in Fig. 4 the strength of the 4-term Chaboche model in simulating multiple-range hysteresis curves, from a very small (RD03) to a very large (RD06) strain range, with reasonable accuracy. Furthermore, the model is able to simulate the responses from experiments RD11, RD12, and RD13, again with reasonable accuracy as shown in Fig. 5a–c. In these figures, it is observed that the responses of different strain ranges with different mean strain-rates are simulated quite reasonably. Again, it is noted that the compressive hysteresis curves are simulated better than the tensile ones.

Table 2
Material parameters used for AA6022-T4.

Type	Parameter	Value
Elasticity	E (MPa)	70,000
	σ_0 (MPa)	50
	ν	0.3
Isotropic hardening	b	10.5
	R_{max} (MPa)	160
Kinematic hardening	C_1 (MPa)	50,000
	C_2 (MPa)	40,000
	C_3 (MPa)	8,500
	C_4 (MPa)	100
	γ_1	900
	γ_2	830
	γ_3	140
	γ_4	0

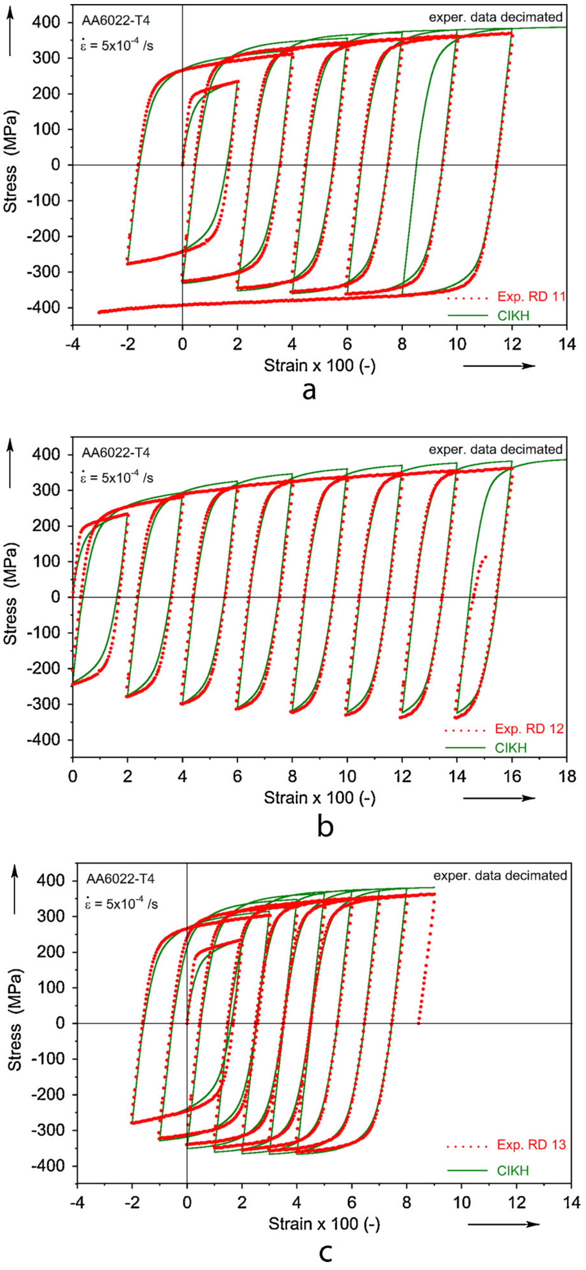

Fig. 5. (a)-(c) Cyclic tension-compression experiments from three different strain histories shown in Fig. 3, and the predictions of the combined isotropic-kinematic hardening model.

This model deficiency lies in the fact that the experimental compressive curves are a little stiffer than the tensile curves, where the simulated curves are of similar stiffness. Also, the modeled behavior near the yield point is under-predicted compared to experimental data for the first cycle, see Fig. 5a–c, but is more accurately predicted in subsequent ones. As presented later, this constitutive model simulates the CBT experimental responses reasonably well and hence no modifications to this model are pursued.

2.4. Post-necking hardening curve

Large strains are anticipated in the CBT process, on the order of, or exceeding, the strains found inside the neck of a tensile specimen (Roemer et al., 2019; Zecevic et al., 2016b). Therefore, the hardening curve that is input in the simulations needs to be identified or extrapolated past the limit of uniform elongation in UT. In this work, the hardening curve is extrapolated assuming that the same parameters of the CIKH model are valid at large strains, see Fig. 6. This assumption is validated later in this work, in Section 3.2.1, by confirming that the predicted crosshead force-displacement curves match the experimental ones. The hardening curve used with IH is identical to that of the CIKH case. Furthermore, the effect of using a different input hardening curve is discussed in Section 3.3. In a parallel effort, the CBT test has been used to identify the hardening curve at large strains (Knezevic et al., 2019).

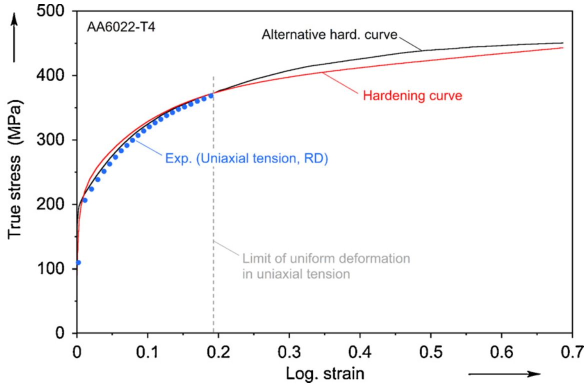

Fig. 6. Hardening curves used in this work, along with uniaxial tension experimental data.

3. Numerical modeling and results

The CBT experiments modeled here are described in detail in (Roemer et al., 2019). For completeness, the key machine, specimen and experiment parameters are repeated here, see Table 3. The experiments were performed on strips extracted from a 1 mm thick AA6022-T4 sheet. The CBT specimen follows the ASTM E-8 geometry, but with an elongated uniform region and gage-length, as listed in Table 3. A major observation from the CBT experiments is that the geometrically uniform region of the specimen sees non-uniform straining in the axial direction: there is a central region (termed 3x) visited by all three rollers during every CBT stroke; adjacent to it are two 2x regions, one on each side; and further out two 1x regions.

3.1. Finite element model of CBT

Figure 7 shows the FE model of the CBT process. The model is created in the implicit code Abaqus/Standard, ver. 6.17. The model consists of three rollers and only half of the specimen, since mirror symmetry is imposed along its length. The rollers are modeled as analytically rigid cylinders of 25.4 mm diameter. The specimen is meshed with linear, reduced integration elements (C3D8R). After suitable parametric studies, a mesh with in-plane dimensions of 0.75 mm x 0.75 mm and 7 elements through the thickness was selected.

Table 3
Summary of key experimental parameters.

Description	Parameter	Value
CBT machine features	L (mm)	54
	D (mm)	25.4
	F_{max} (kN)	312
	Stroke (mm)	305
CBT specimen geometry	t (mm)	1
	Gage length (mm)	190
	Gage width (mm)	12
CBT process parameters	v_{CH} (mm/s)	1.2
	v_{R} (mm/s)	66
	δ (mm)	2.5

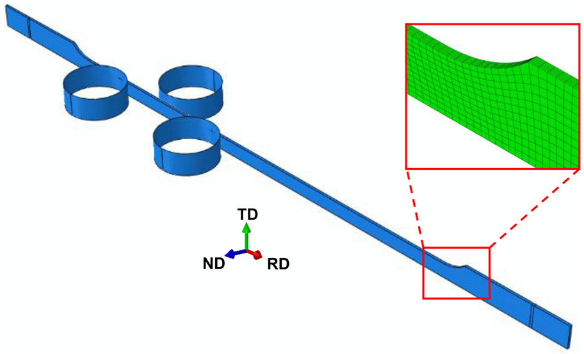

Fig. 7. Finite element model of CBT, also showing the mesh in an inset.

These in-plane dimensions are refined enough to follow the profile of the rollers, and a sufficient number of integration points (7) is available to capture the bending effects. Reduced integration elements in bending are prone to a non-physical, zero-energy mode of deformation referred to as hourglassing. In order to suppress this non-physical mode of deformation while maintaining a low amount of artificial strain energy added to the system, the enhanced hourglass control available in Abaqus is utilized. The total number of elements is 33,516. A snapshot of the mesh is included in Fig. 7.

Contact is enforced using the default state-based tracking, which precludes penetration of the specimen nodes into the surface of the rollers. Roller-specimen friction is assumed to be of Coulomb-type, with a friction coefficient of $\mu = 0.17$ (dry friction, as no lubricant was used in our experiments), (Roemer et al., 2019).

The simulations are designed to match the experiment as closely as possible. Bending is applied by displacing the center roller to a bending depth of $\delta = 2.5$ mm, see Fig. 1. The rollers are free to rotate while they are reciprocated along the length of the specimen with a velocity of $V_R = 66$ mm/s, as in the experiments (Roemer et al., 2019). The stroke of the rollers covers the gage section and changes with every cycle. This roller stroke data was recorded experimentally (Roemer et al., 2019) and imported into the model. The gripped regions on either end of the specimen are assumed to be rigid. Initially, both gripped regions are held stationary. After the pre-strain cycle has been completed, a crosshead velocity of $V_{CH} = 1.2$ mm/s is applied to one side of the specimen.

The simulations utilize the CIKH material model described in Section 2.2 and the hardening curve in Section 2.4. For comparison purposes, simulations with the default IH assumption were also performed and their predictions will be compared to those of CIKH.

3.2. Numerical results and comparison to experiments

3.2.1. Crosshead force-displacement

The numerical model is now exercised to predict the response of the material during CBT, as well as to help understand the mechanics of the process. The first quantity of interest is the crosshead force-displacement response, shown in Fig. 8. The experimentally observed succession of force spikes and plateaus is reproduced well, by both the IH and CIKH models. This is an indication that the extrapolation of the hardening curve (Section 2.4) is appropriate to capture the material behavior at high strain values. This is especially true at larger strains, where the two curves match. Also identified in that figure are the values of equivalent plastic strain. The strain at uniform elongation, which is approx. 0.2 is reached during the first 1/3 of the CBT process. Beyond that, significantly larger strains develop (e.g., over 0.45 peak strain is shown in Fig. 8, i.e., twice that in uniform elongation), which is the result of suppressing the necking instability. During this work, it was also observed that the accuracy of the model with respect to the CBT experiments was dependent on the post-necking hardening curve used, see Fig. 6. Indeed, this observation has been used in our earlier work to inversely-identify the hardening curve (Knezevic et al., 2019).

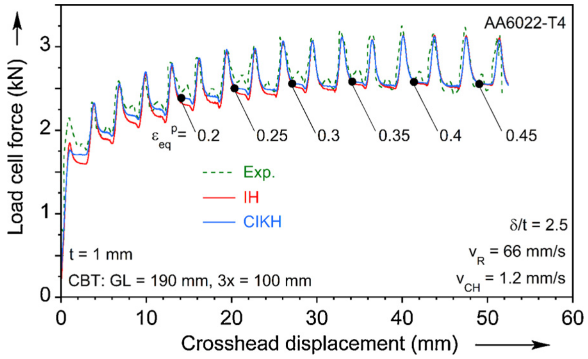

Fig. 8. Crosshead force-displacement during CBT, showing the experiment and the predictions of isotropic and combined isotropic-kinematic hardening. Also included are values of equivalent plastic strain (von Mises) during the process.

3.2.2. Strain paths during CBT

The strain development during CBT can be now compared to the predictions, in a variety of different formats. Shown in Fig. 9 are the surface strains found along the length of a CBT specimen after 8.5 cycles, as well as the corresponding IH and CIKH predictions. Also included is the strain path traced by a single material point during UT. From this comparison, it can be concluded that the strains found on the surface of a CBT specimen are very close to those observed in UT. Some limited shifting towards plane-strain tension can be seen, as discussed in (Emmens, 2011; Emmens and van den Boogaard, 2011). This is further corroborated by Fig. 10, where the strain paths traced by two material points, one in the 2x region and the other in the 3x one (Roemer et al., 2019), are shown along with the strains along a CBT specimen, and the strain path during UT. (The 3x central region of the CBT specimen is visited by all three rollers during a CBT stroke, and hence undergoes 3 bending-unbending cycles, while the adjacent 2x regions, are only visited by two instead of the three rollers (Roemer et al., 2019).) In every case, the simulations confirm that the strain

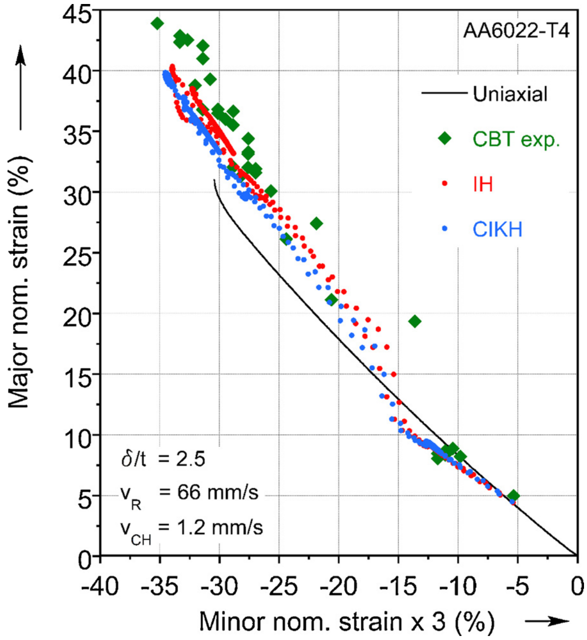

Fig. 9. Major and minor in-plane strains along the final CBT specimen, from experiment and the two material models. Included is the strain path from uniaxial tension. The x-axis is multiplied by 3 to enhance clarity.

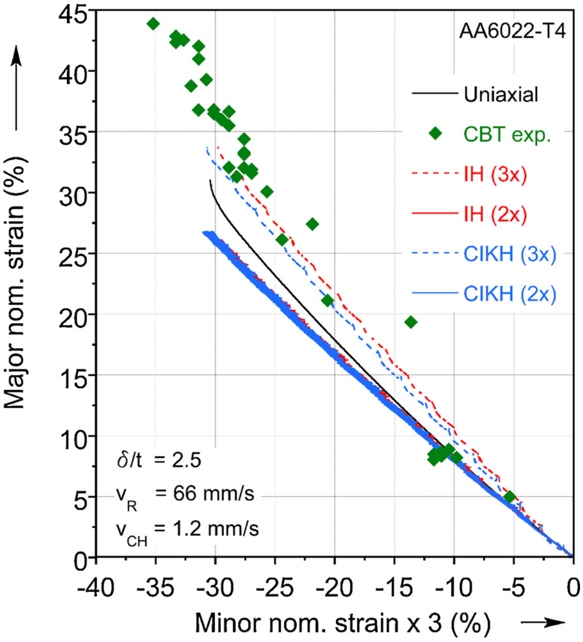

Fig. 10. Strain paths during the CBT process in two regions (2x and 3x) from the two material models. Included is the strain path from uniaxial tension, and the strains measured on the final CBT specimen. The x-axis is multiplied by 3 to enhance clarity.

development during CBT is comparable to that in UT, as in our earlier observations (Roemer, 2016; Roemer et al., 2019; Zecevic et al., 2016b). The difference in the IH and CIKH predictions is minimal, indicating the limited amount of kinematic hardening that this material exhibits.

3.2.3. *Strain development along a CBT specimen*

The development of surface strain during CBT is shown in Fig. 11. Added to the predictions of IH and CIKH are experiments using, a) width and thickness measurements and b) circle-grid analysis, on both a UT and a CBT specimen (Roemer et al., 2019). The numerical results reproduce the experiments very well, including the appearance of the 1x, 2x and 3x regions, as well as the locally increased strains at the transition between the 2x and 3x regions, where failure occurs in CBT. As in earlier reports, the strains in the 3x region of CBT are comparable to the maximum strains found in UT (Roemer et al., 2019; Zecevic et al., 2016b). In concert with the findings reported above, the predictions of IH and CIKH are essentially identical.

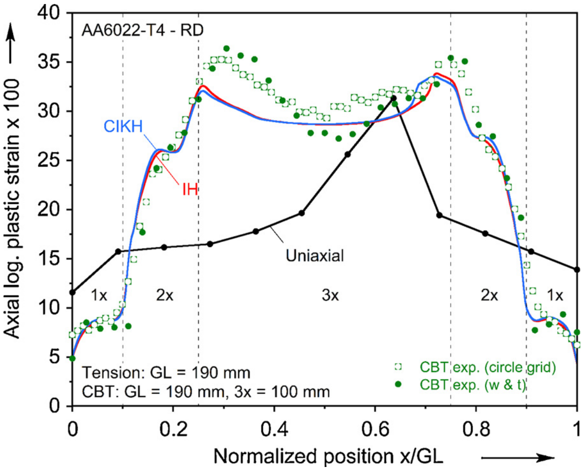

Fig. 11. Axial strain distribution along the final CBT specimen, including measurements by two methods and predictions from the two material models. Included is the uniaxial tension measurement.

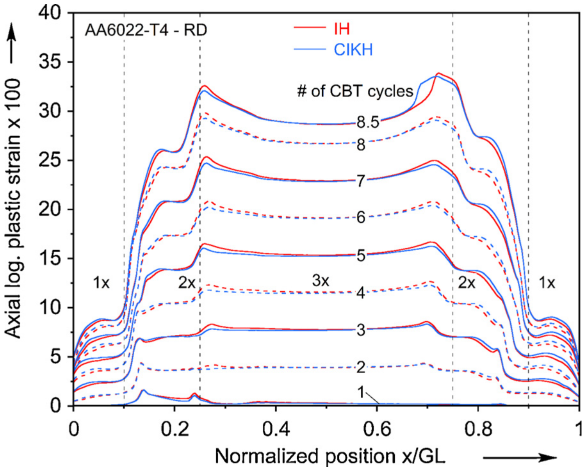

Fig. 12. Evolution of axial strain during CBT as predicted by the two material models.

A similar conclusion can be drawn by looking at Fig. 12, which shows the accumulation of plastic strain during CBT. Throughout loading, the results of IH and CIKH are very similar. Each CBT cycle seems to add a fixed amount of plastic strain in the 3x region. On the other hand, during the early stages of CBT, the strain difference between the 2x and 3x regions is not that significant. However, the increased strain at the boundary of the 2x and 3x regions appears early on and seems to grow with every CBT cycle. This locally increased strain may be attributed to the deceleration and acceleration in the reverse direction at the end of each CBT stroke. (The profile of the relative velocity between roller and specimen is given in Fig. 8 in (Roemer et al., 2019).) During that time, the crosshead continues to stretch the specimen, which preferentially deforms in the region of the roller closest to the crosshead. The deformation changes during this time from the superposition of bending, tension and contact stresses to that of simply uniaxial tension. This induces local flow of the material, before the rollers have again started to move, in the reverse direction.

3.2.4. *Strain accumulation at a point during CBT*

The numerical model can also be used to shed light into the stress and strain distributions through the thickness of the specimen. The evolution of axial strain at two material (or interrogation) points at the center of the specimen (i.e., inside the 3x region) and at the opposite (top and bottom) surfaces is shown in Fig. 13. These results are

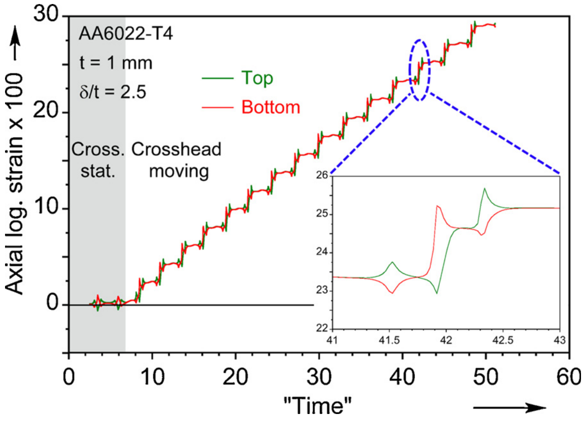

Fig. 13. Axial strain evolution at the top and bottom surfaces at the center of the CBT specimen, mid-width. (Note: "time" here is a monotonically and linearly increasing simulation parameter, i.e., it has no physical meaning.).

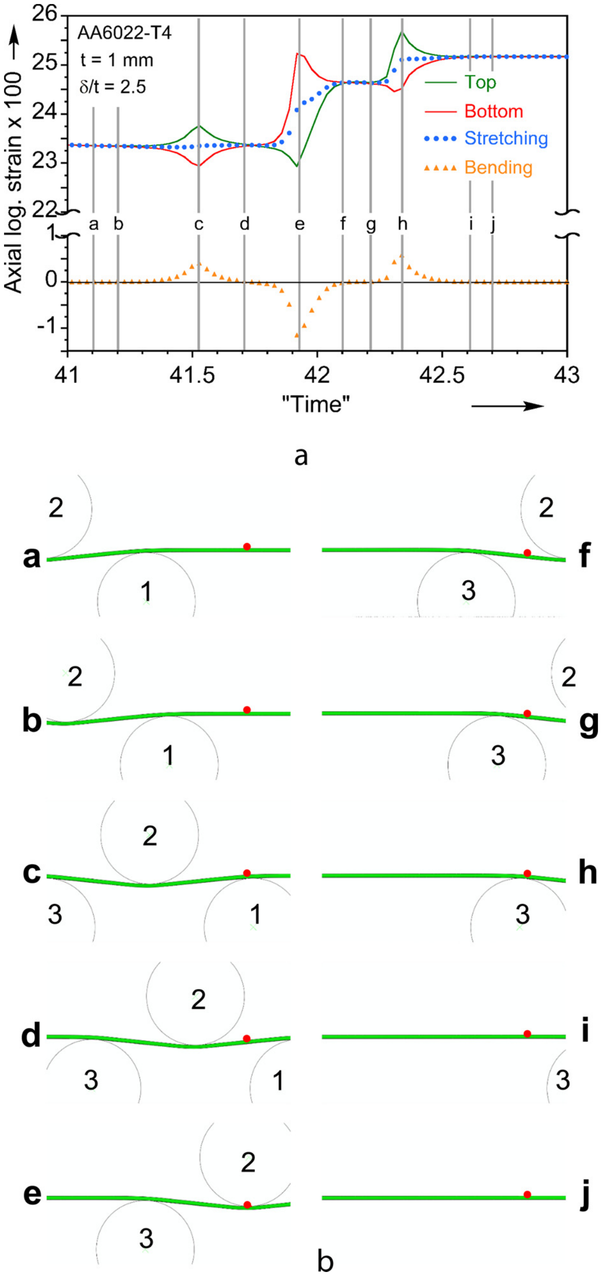

Fig. 14. (a) Magnified view of the strain at the center of a CBT specimen and at mid-width, during 10 instances ("a"-"j") and a specific CBT stroke. Included are the stretching ((top + bottom)/2) and bending ((top - bottom)/2) components of the strain. (b) Schematic to identify the location of the interrogation point for instances "a"-"j". The point, which is the center of the CBT specimen, is identified with a dot in every instance. The three rollers are numbered as 1-2-3. (Note: "time" here is a monotonically and linearly increasing simulation parameter, i.e., it has no physical meaning.).

obtained from the CIKH material model, as they are identical to the IH ones. In the beginning of the graph, the crosshead is stationary for 1 CBT cycle. This approach was used experimentally to allow all sensors to initialize, ensure that the specimen is properly secured, and yield more reproducible experiments. It can be seen that the strain accumulates in a staircase fashion, with a pattern of 3 spikes (see inset of Fig. 13) occurring every time the rollers pass through the interrogation points at the center of the specimen. Outside of that time, the strain remains constant, verifying that the dominant mode of deformation in CBT is the superposition of bending on tension. This mechanism is further elucidated in Fig. 14. The inset of Fig. 13 is shown in Fig. 14a, along with the stretching (solid circles) and bending (solid triangles) components. These are obtained as the "mean-value" and "amplitude" of the top and bottom strains, respectively, with the wording based on an analogy with a periodic, oscillating function. The underlying assumption for extracting the axial strain due to bending as the "amplitude" is the symmetry between tension and compression. The assumption is reasonable for relatively symmetric metals with cubic structure, while it would be violated for hexagonal metals (Knezevic et al., 2013).

Identified with solid vertical lines in Fig. 14a are specific instances, which correspond to the position of the interrogation points to the rollers (numbered as 1, 2 and 3), as detailed in Fig. 14b. At instances "a" and "b", the rollers are approaching the points, both of which have the same strain, equal to the stretching strain (i.e., zero bending strain). As the rollers approach, the strain remains unchanged. At instance "c", the point is on top of the leading roller, and experiences bending. Interestingly, the stretching strain remains almost unchanged. At "d", the points have been unbent, essentially to the original strain. However, at "e", the points are under the center roller and have experienced reverse bending, and indeed significantly greater strain than over the leading roller. In that process, both the stretching and bending strains increase significantly. At "f" and "g" the reverse bending is removed and the bending strain is zero. At "h", the points are bent again, over the trailing roller. In contrast to the first bending, that process induces both stretching and bending strains. Finally, at "i" and "j" the top and bottom points have the same strain, and all bending has been removed. At the same time, the further increase of strain has been halted.

The results of Fig. 14 reveal the physics of the CBT process. The fact that the maximum bending strains at the leading and trailing roller (i.e., at "c" and "h") are lower, in absolute value, than the bending strain induced by the center roller (i.e., at "e") indicates insufficient wrapping of the specimen on the rollers, which is discussed below. Furthermore, none of these is approaching the design value of the bending strain in this experimental set-up (i.e., for 1 mm-thick specimen and 25 mm dia. rollers, the nominal bending strain should be $t/(D + t)$, where t is the material thickness and D is the diameter of the roller, see Fig. 1, i.e., 3.8 % here, while the log. strains x 100 at "c", "e" and "h" are 0.4 %, 1.85 % and 1%, respectively).

The insufficient wrapping is further illustrated in Fig. 15. Fig. 15a shows a vector plot of the out-of-plane displacement of the specimen in the direction opposite to the bending depth. (Note that for clarity, the limits are selected such that no displacement vectors are visible in the direction of that depth). A plot of this displacement at different instances throughout a CBT stroke is given in Fig. 15b. From both plots, it can be concluded that the lift-off of the specimen on the leading and trailing rollers is different, with the latter being always greater. This explains why larger strains are induced during that bending, rather than the one at the leading roller.

The insufficient wrapping indicates that the specimen "rides over" the leading roller, trying to accommodate the enforced change in direction by minimal deformation (bending over a large region, i.e., with small curvature, certainly much smaller than the inverse of the roller radius). However, the specimen is forced to wrap tighter around the center roller to accommodate its change of direction, which imparts a relatively large increase in both stretching and bending. Finally, the specimen is also riding over the trailing roller. The greater out-of-plane displacement in comparison to that at the leading roller leads to larger strains being induced to return the specimen to the original, flat configuration.

In retrospect, increasing the crosshead velocity relative to the roller one could result in better wrapping of the specimen around the rollers, especially the leading one. The same of course could be accomplished by increasing the (normalized) bending depth, δ/t, see Fig. 1.

Additional information can be extracted by studying the plastic, instead of total, strains, see Fig. 16. From the inset of Fig. 16a it can be seen that the plastic strain at the top and bottom surface is not the same,

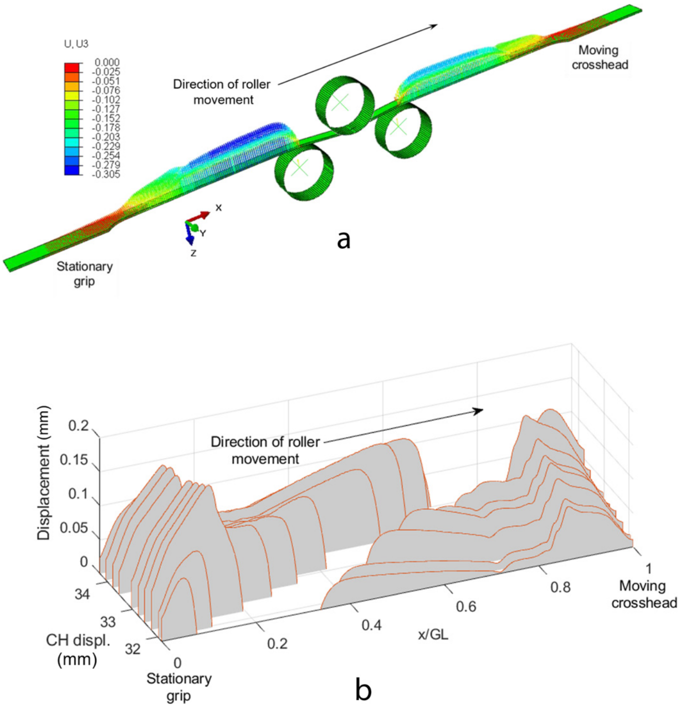

Fig. 15. (a) Out-of-plane displacement during a CBT stroke, indicating the asymmetry discussed in the text. The scale is starting from zero, to highlight this asymmetry. (b) Plot of the out-of-plane displacement along the (normalized) specimen length during a CBT stroke.

which implies that the deformed specimen will have residual curvature (springback) upon release from the testing machine, as is confirmed experimentally. The inset is magnified in Fig. 16b, which also includes the stretching and bending components of the plastic strain. It is interesting to note that at “a” there is already plastic bending strain, which is a consequence of prior CBT cycles. Furthermore, engaging the first (i.e., leading) roller results in purely elastic bending, with no plasticity induced (point “c”). Engaging the center and trailing rollers increases the plastic strain (points “e” to “h”). After the rollers depart (points “i” and “j”), both the stretching and bending plastic strains have increased in comparison to the beginning of the process. The increase of plastic bending strain implies an increase in springback, as the CBT process continues.

3.2.5. *Stress and strain development through-thickness*

Additional information on the mechanics of the CBT process are provided by examining the stress and strain distributions inside the specimen. The axial log. strain distribution at the center of the specimen for the instances “a” to “j” is given in Fig. 17a. Both the total and the plastic strains are included. Discussing the total strain first, it can be seen that before the leading roller arrives at that position along the specimen (at “a” and “b”) the strain remains essentially constant. Then, as the material points pass over the leading roller (at “c”), a bending strain distribution with stretching on the top surface and contracting on the bottom is experienced. While perhaps difficult to establish from this 3D view, upon inspection the strain distribution is found to be close to linear. Then, at “d” the specimen is almost straight again, before it experiences reverse bending while passing the center roller (at “e”). Then straight at “f” and “g”, forward bending at “h” and straight again at “i” and “j”. The amount of bending imparted at “e” and “h” (i.e., center and trailing rollers) is significantly more than at “c” (i.e., leading roller).

The plastic strains are also included in Fig. 17a. It is noted again that the plastic strain is different at the top and bottom surfaces before any engagement with the rollers, i.e., at “a” and “b”. This is consistent with the result shown earlier, in Fig. 16b. It is interesting to note that bending at the leading roller (at “c”) is elastic, so that at “d” the plastic strain distribution is the same as at “a” and “b”. A significant amount of plasticity is induced at “e” (bending over the center roller), with a pronounced bending character. Interestingly, stretching is added between “e” and “f”, see Fig. 14a, and some additional plastic strain from bending over the trailing roller is induced at “h”. After additional stretching (from the crosshead), the achieved strain level at “i” is the same as at “j”.

The true stress distribution is shown in Fig. 17b. While the total strain plots are close to linear, to be expected since the amounts of bending are limited, the stresses are completely non-linear. The engagement with the 3 rollers is clearly seen as altering the through-thickness distribution of the stress. Points “a” and “b” are outside of the roller engagement and exhibit a non-uniform stress distribution due to previous CBT cycles. The bending stress seen at point “c” is almost entirely elastic as it returns to the same stress state afterwards at point “d” as it was at point “b”. A significant change in the through-thickness stress profile occurs at point “e” when the material is directly underneath the middle roller, thus experiencing plastic flow due to bending. Subsequent unbending and bending is seen at points “f” and “g” resulting in a small amount of additional plastic flow. Despite being under the trailing roller, the stress profile of point “h” is consistent with that of “f” and “g” but with some additional bending stress added. Beyond that at points “i" and “j”, the resulting stress profile is consistent in shape but has increased in magnitude as compared to points “a” and “b” due to CBT processing. It is interesting to note that the through-thickness stresses can include a compressive component, so that the net axial force can be lower than the maximum force that the specimen can sustain under UT. This reveals the reason for enhanced elongation in CBT, over UT (Momanyi et al., 2017; Poulin et al., 2019; Roemer et al., 2019; Zecevic et al., 2016b).

3.2.6. *Some observations on failure in CBT*

The numerical results reproduce the experimental observation of the failure location, i.e., that the maximum strain accumulation develops at the boundary between the 2x and 3x regions, e.g., Figs. 11 and 12. By observing the evolution of strain accumulation during the process, it is clear that this strain concentration is present throughout the

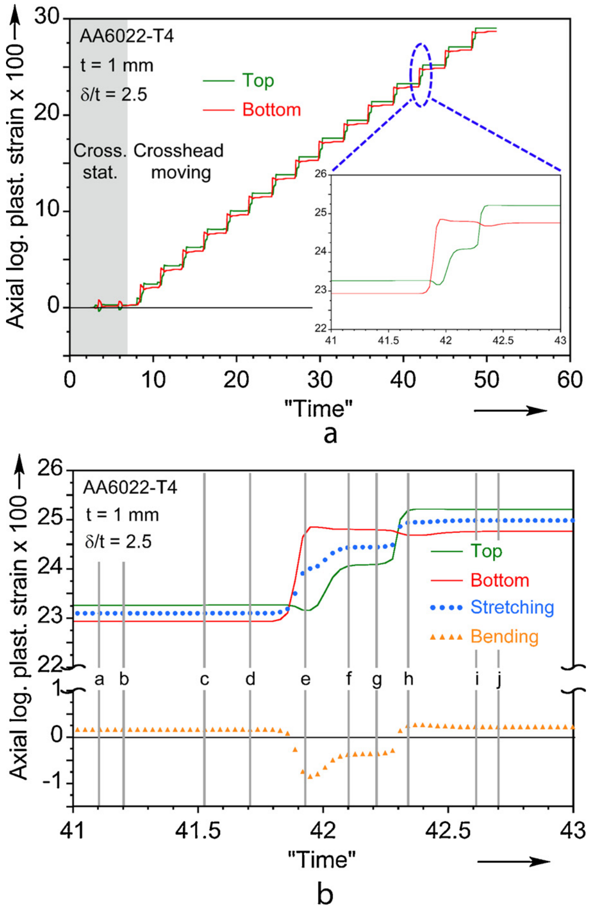

Fig. 16. (a) Evolution of plastic strain during the CBT process. (b) Magnified view of the plastic strain at the center of a CBT specimen during the 10 instances identified in Fig. 14b, and a specific CBT stroke. Included are the stretching and bending components of the plastic strain. (Note: "time" here is a monotonically and linearly increasing simulation parameter, i.e., it has no physical meaning.).

CBT process (Fig. 12). Following the discussions in the preceding sections, this can be explained as follows: the wrapping of the specimen on the trailing roller is incomplete. Therefore, at the end of each stroke, the part of the specimen between the trailing roller and the grip consists of a straight section and the curved one, over the roller. As the rollers have stopped moving, that section is submitted to stretching, which is accommodated by additional bending of the curved region, to conform to the curvature of the roller. This process ceases, as soon as the rollers start moving in the opposite direction. It is however enough to induce some additional plasticity behind the trailing roller, i.e., at the 2x-3x boundary, which is what is shown in Fig. 12.

The numerical results also reveal that the kinematics of the CBT process force the band of maximum strain accumulation to appear along the width of the specimen. Therefore, it is not surprising that the rupture of the specimen in CBT occurs along the width, i.e., perpendicular to the major principal stress. This is in contrast to the rupture along the plane-strain direction, i.e., that of a localized neck, as is typical in rupture in UT.

3.3. Sensitivity of the results to the input hardening curve

The numerical model also enables an investigation of the effect of the hardening curve that is input to the simulation, to the predictions. For this purpose, and given that for the current hardening curve, see Fig. 6, the IH and CIKH results are essentially identical, the IH model was paired with a different hardening curve, shown in Fig. 6 with a black solid line. The results for the force-displacement predictions are shown in Fig. 18. The curves are slightly different at low displacements (and thus strains), as are the hardening curves in Fig. 6; they then are on top of each other at mid-range, while they start to again deviate from each other at large displacements/strains. This indicates a sensitivity of these predictions to the hardening curve that is input in the simulations. In turn, it indicates that CBT can be used to identify the hardening curve at large strains, as has been pursued by the authors (Knezevic et al., 2019).

4. Summary and conclusions

In this paper, simulations of the CBT process were described. First, the cyclic behavior of the material was probed under a variety of strain histories. Some of the experiments were used to calibrate a CIKH model, which was shown to match the remainder of the responses very well. As loading in CBT is primarily along a single direction, use of a von Mises yield function was found to be sufficient, and hence an anisotropic yield function was not needed. This material model (i.e., CIKH & von Mises), along with standard IH was implemented in a FE model of CBT. The predictions of the crosshead force-displacement and of strains for the final specimen were found to be in good agreement with the experiments. No significant difference in the predictions of IH and CIKH was found for this material. Subsequently, the model was used to investigate the strain development during CBT, as well as the stress and strain evolution at a point and per cycle. Finally, observations of failure, and of the sensitivity of the results to the hardening curve input to the simulations were discussed.

From the model results, it can be concluded that the strain evolution during CBT occurs in a staircase pattern, increasing only during roller engagement. This verifies the working assumption behind CBT, that the material deforms only through a superposition of tension and bending. Since the plastic strains at the top and bottom surfaces of the specimen were found to be unequal, the springback observed when the specimen is removed from the machine can be explained. The simulations also revealed that the maximum strain in CBT develops at the boundary of the 2x and 3x regions, where failure is observed experimentally. Furthermore, the distributions of stress and strain through the thickness and at interrogation points around the rollers, as well as the simulated vertical displacements and wrapping of the material on the rollers, help explain the kinematics and phenomena observed in the CBT process. Finally, the amount of kinematic hardening is limited for this material, so that the predictions of the CIKH material model largely match those of IH. On the other hand, the results are sensitive to the input hardening curve, so that the CBT process can be used for identifying the hardening curve at large strains.

CRediT authorship contribution statement

Timothy J. Barrett: Methodology, Software, Formal analysis, Investigation, Visualization, Writing - original draft. **Shuhei Takagi:** Investigation, Formal analysis, Writing - review & editing. **Nazrul Islam:** Investigation, Formal analysis, Writing - review & editing. **Toshihiko Kuwabara:** Formal analysis, Writing - review & editing. **Tasnim Hassan:** Formal analysis, Writing - review & editing. **Brad L. Kinsey:** Methodology, Conceptualization, Formal analysis, Funding acquisition, Writing - review & editing. **Marko Knezevic:** Methodology, Conceptualization, Formal analysis, Funding acquisition, Writing - review & editing. **Yannis P. Korkolis:** Methodology, Conceptualization, Formal analysis, Visualization, Funding acquisition, Writing - original draft.

Declaration of Competing Interest

The authors declare that they have no known competing financial interests or personal relationships that could have appeared to

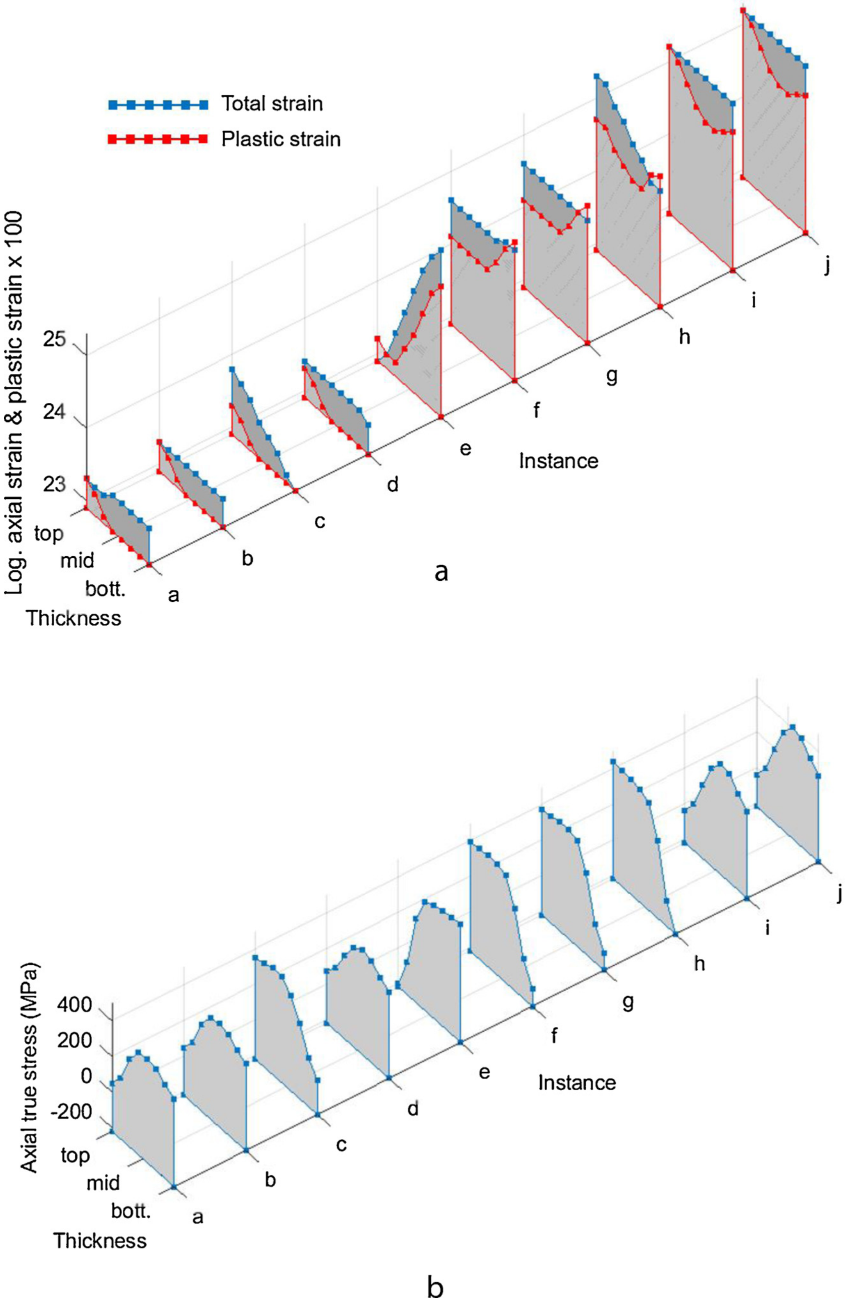

Fig. 17. (a) Through-thickness distribution of axial strain and plastic strain in the 10 instances "a"-"j" identified in Fig. 14b. (b) Same, for the axial stress.

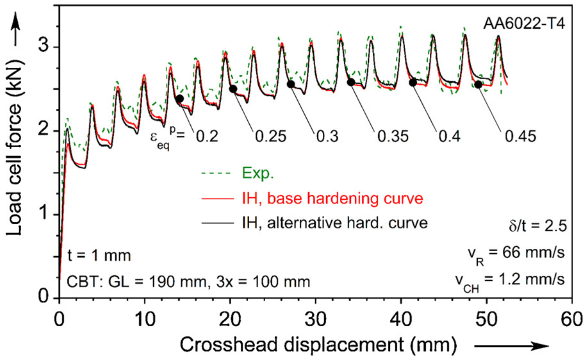

Fig. 18. Prediction of the crosshead force-displacement for two different hardening curves (see Fig. 6) used with isotropic hardening, indicating a deviation at large strains.

influence the work reported in this paper.

Acknowledgements

This research was partially supported by the U.S. National Science Foundation (grant CMMI-1301081). We acknowledge the support of Dr. Cedric Xia, formerly of Ford Motor Co., on developing the experimental CBT apparatus and Dr. Joe Benedyk, the inventor of CBT, for his interest in our work. YK would like to thank Dr. Patrick Duroux of Arcelor-Mittal for his insightful comments on stresses and strains in a thin sheet flowing over radii. YK also gratefully acknowledges the support of the Global Innovation Research Organization in TUAT for this article. TB and MK are grateful for financial support to the U.S. National Science Foundation under the CAREER grant no. CMMI-1650641.

References

Bari, S., Hassan, T., 2000. Anatomy of coupled constitutive models for ratcheting simulation. Int. J. Plast. 16, 381–409. https://doi.org/10.1016/S0749-6419(99)00059-5.

Benedyk, J.C., Stawarz, D., Parikh, N.M., 1971. A method for increasing elongation values for ferrous and nonferrous sheet metals. J. Mater. 6, 16–29.

Benedyk, J.C., Mostovoy, S., Janota, R., 2002. “The continuous bending under tension (CBT) test method for evaluating formability of sheet metal”. Light Met. Age 60, 6–9.

Benedyk, J.C., Kinsey, B.L., Korkolis, Y.P., Roemer, T.J., 2015. Fundamental studies of continuous bending under tension (CBT) and potential automotive forming applications. Materials Today: Proceedings. https://doi.org/10.1016/j.matpr.2015.10.089.

Boger, R.K., Wagoner, R.H., Barlat, F., Lee, M.G., Chung, K., 2005. Continuous, large strain, tension/compression testing of sheet material. Int. J. Plast. 21, 2319–2343. https://doi.org/10.1016/j.ijplas.2004.12.002.

Cao, J., Lee, W., Cheng, H.S., Seniw, M., Wang, H.-P., Chung, K., 2009. Experimental and numerical investigation of combined isotropic-kinematic hardening behavior of sheet metals. Int. J. Plast. 25, 942–972.

Chaboche, J.L., 1986. Time-independent constitutive theories for cyclic plasticity. Int. J. Plast. 2, 149–188. https://doi.org/10.1016/0749-6419(86)90010-0.

Chung, K., Lee, M.-G., Kim, D., Kim, C., Wenner, M.L., Barlat, F., 2005. Spring-back evaluation of automotive sheets based on isotropic-kinematic hardening laws and non-quadratic anisotropic yield functions. Int. J. Plast. 21, 861–882. https://doi.org/10.1016/j.ijplas.2004.05.016.

Dafalias, Y.F., Popov, E.P., 1975. A model of nonlinearly hardening materials for complex loading. Acta Mech. 21, 173–192.

Deng, N., Kuwabara, T., Korkolis, Y.P., 2018. On the non-linear unloading behavior of a biaxially loaded dual-phase steel sheet. Int. J. Mech. Sci. 138–139, 383–397. https://doi.org/10.1016/J.IJMECSCI.2018.02.015.

Emmens, W.C., 2011. Formability: A Review of Parameters and Processes that Control, Limit or Enhance the Formability of Sheet Metal. Springer-Verlag, Berlin Heidelberg.

Emmens, W.C., van den Boogaard, A.H., 2009. Incremental forming by continuous bending under tension-An experimental investigation. J. Mater. Process. Technol. 209, 5456–5463. https://doi.org/10.1016/j.jmatprotec.2009.04.023.

Emmens, W.C., van den Boogaard, A.H., 2011. Cyclic stretch-bending: mechanics, stability and formability. J. Mater. Process. Technol. 211, 1965–1981. https://doi.org/10.1016/j.jmatprotec.2011.06.017.

Emmens, W.C., van den Boogaard, A.H., 2012. Material characterization at high strain by adapted tensile tests. Exp. Mech. 52, 1195–1209. https://doi.org/10.1007/s11340-011-9577-x.

Geng, L., Shen, Y., Wagoner, R.H., 2002. Anisotropic hardening equations derived from reverse-bend testing. Int. J. Plast. 18, 743–767. https://doi.org/10.1016/S0749-6419(01)00048-1.

Hadoush, A., van den Boogaard, A.H., Emmens, W.C., 2011. A numerical investigation of the continuous bending under tension test. J. Mater. Process. Technol. 211, 1948–1956. https://doi.org/10.1016/j.jmatprotec.2011.06.013.

Hassan, T., Kyriakides, S., 1992. Ratcheting in cyclic plasticity, part I: uniaxial behavior. Int. J. Plast. 8, 91–116.

Hassan, T., Corona, E., Kyriakides, S., 1992. Ratcheting in cyclic plasticity, part II: multiaxial behavior. Int. J. Plast. 8, 117–146.

Hu, J., Marciniak, Z., Duncan, J., 2002. Mechanics of Sheet Metal Forming. Elsevier.

Knezevic, M., Lebensohn, R.A., Cazacu, O., Revil-Baudard, B., Proust, G., Vogel, S.C., Nixon, M.E., 2013. Modeling bending of α-titanium with embedded polycrystal plasticity in implicit finite elements. Mater. Sci. Eng. A 564, 116–126. https://doi.org/10.1016/j.msea.2012.11.037.

Knezevic, M., Poulin, C.M., Zheng, X., Zheng, S., Beyerlein, I.J., 2019. Strengthening of alloy AA6022-T4 by continuous bending under tension. Mater. Sci. Eng. A 758, 47–55. https://doi.org/10.1016/j.msea.2019.04.109.

Kuwabara, T., 2014. Biaxial stress testing methods for sheet metals. Comprehensive Materials Processing. https://doi.org/10.1016/B978-0-08-096532-1.00106-0.

Lee, M.-G., Kim, D., Kim, C., Wenner, M.L., Chung, K., 2005. Spring-back evaluation of automotive sheets based on isotropic–kinematic hardening laws and non-quadratic anisotropic yield functions, part III: applications. Int. J. Plast. 21, 915–953. https://doi.org/10.1016/j.ijplas.2004.05.014.

Lemaitre, J., Chaboche, J.-L., 1990. Mechanics of Solid Materials. Cambridge University Press, Cambridge. https://doi.org/10.1017/CBO9781139167970.

Marciniak, Z., Kuczyński, K., 1967. Limit strains in the processes of stretch-forming sheet metal. Int. J. Mech. Sci. 9, 609–620. https://doi.org/10.1016/0020-7403(67)90066-5.

Marciniak, Z., Kuczyński, K., 1979. The forming limit curve for bending processes. Int. J. Mech. Sci. 21, 609–621. https://doi.org/10.1016/0020-7403(79)90081-X.

Momanyi, E.M., Roemer, T.J., Kinsey, B.L., Korkolis, Y.P., 2017. Experimental investigation of key process parameters during continuous-bending-under-tension of AA6022-T4. ASME 2017 12th International Manufacturing Science and Engineering Conference, MSEC 2017 Collocated with the JSME/ASME 2017 6th International Conference on Materials and Processing. https://doi.org/10.1115/MSEC20173045.

Nikhare, C., Kinsey, B.L., Korkolis, Y., 2012. Numerical investigation of residual formability and deformation localization during continuous-bending-under-tension. In: ASME 2012 International Manufacturing Science and Engineering Conference Collocated with the 40th North American Manufacturing Research Conference and in Participation with the Int. Conf. MSEC 2012. https://doi.org/10.1115/MSEC2012-7302.

Piao, K., Lee, J.K., Kim, J.H., Kim, H.Y., Chung, K., Barlat, F., Wagoner, R.H., 2012. A sheet tension/compression test for elevated temperature. Int. J. Plast. 38, 27–46. https://doi.org/10.1016/j.ijplas.2012.03.009.

Poulin, C.M., Korkolis, Y.P., Kinsey, B.L., Knezevic, M., 2019. Over five-times improved elongation-to-fracture of dual-phase 1180 steel by continuous-bending-under-tension. Mater. Des. 161, 95–105. https://doi.org/10.1016/j.matdes.2018.11.022.

Roemer, T.J., 2016. Experimental Apparatus for Continuous-Bending-Under-Tension and Experiments on AA6022-T4. University of New Hampshire.

Roemer, T.J., Kinsey, B.L., Korkolis, Y.P., 2015. Design of a continuous-bending-under-tension machine and initial experiments on AL-6022-T4. In: ASME 2015 International Manufacturing Science and Engineering Conference. MSEC 2015. https://doi.org/10.1115/MSEC20159440.

Roemer, T.J., Barrett, T.J., Knezevic, M., Kinsey, B.L., Korkolis, Y.P., 2019. Experimental study of continuous-bending-under-tension of AA6022-T4. J. Mater. Process. Technol. 266, 707–714. https://doi.org/10.1016/j.jmatprotec.2018.11.046.

Yao, H., Cao, J., 2002. Prediction of forming limit curves using an anisotropic yield function with prestrain induced backstress. Int. J. Plast. 18, 1013–1038.

Yoshida, F., Uemori, T., 2002. A model of large-strain cyclic plasticity describing the Bauschinger effect and workhardening stagnation. Int. J. Plast. 18, 661–686. https://doi.org/10.1016/S0749-6419(01)00050-X.

Yoshida, F., Uemori, T., Fujiwara, K., 2002. Elastic–plastic behavior of steel sheets under in-plane cyclic tension–compression at large strain. Int. J. Plast. 18, 633–659. https://doi.org/10.1016/S0749-6419(01)00049-3.

Zecevic, M., Korkolis, Y.P., Kuwabara, T., Knezevic, M., 2016a. Dual-phase steel sheets under cyclic tension–compression to large strains: experiments and crystal plasticity modeling. J. Mech. Phys. Solids 96. https://doi.org/10.1016/j.jmps.2016.07.003.

Zecevic, M., Roemer, T.J., Knezevic, M., Korkolis, Y.P., Kinsey, B.L., 2016b. Residual ductility and microstructural evolution in Continuous-Bending-under-Tension of AA-6022-T4. Materials (Basel) 9. https://doi.org/10.3390/ma9030130.